

Mapping the energy surface of PbTiO_3 in multidimensional electric-displacement space

Jiawang Hong* and David Vanderbilt

Department of Physics and Astronomy, Rutgers University, Piscataway, NJ 08854-8019, USA

(Dated: September 19, 2011)

In recent years, methods have been developed that allow first-principles electronic-structure calculations to be carried out under conditions of fixed electric field. For some purposes, however, it is more convenient to work at fixed electric displacement field. Initial implementations of the fixed-displacement-field approach have been limited to constraining the field along one spatial dimension only. Here, we generalize this approach to treat the full three-dimensional displacement field as a constraint, and compute the internal-energy landscape as a function of this multidimensional displacement-field vector. Using PbTiO_3 as a prototypical system, we identify stable or metastable tetragonal, orthorhombic and rhombohedral structures as the displacement field evolves along [001], [110] and [111] directions, respectively. The energy minimum along [001] is found to be deeper than that along [110] or [111], as expected for a system having a tetragonal ground state. The barriers connecting these minima are found to be quite small, consistent with the current understanding that the large piezoelectric effects in PbTiO_3 arise from the easy rotation of the polarization vector.

PACS numbers: 77.80.-e, 71.15.-m

I. INTRODUCTION

Since their introduction almost a decade ago,^{1,2} methods for carrying out first-principles electronic-structure calculations under conditions of fixed electric field \mathcal{E} have found wide application in the study of the dielectric, piezoelectric, and ferroelectric behavior of materials.³⁻⁶ More recently, variants of this approach, in which the electric polarization⁷ or the electric displacement field⁸ is taken as the fundamental variable instead, have been introduced. Fixing the displacement field D has the intuitive interpretation of imposing open-circuit electrical boundary conditions, which is often especially useful for studying layered geometries such as metal-oxide interfaces^{9,10} and ferroelectric capacitors¹¹ and superlattices.^{12,13}

There are several reasons why the fixed- D approach is advantageous for such applications. In a superlattice structure, the local polarization P and electric field \mathcal{E} can vary from one layer to another, so their overall spatial average is not a fundamental quantity. In contrast, D is constant throughout the system, since free charge is assumed to be absent. (Here, \mathcal{E} , P and D refer to the field components in the stacking direction.) Therefore, choosing D as the fundamental electrical variable is especially practical because it makes it possible to decompose the equation of state of a layered structure into the sum of contributions from the individual building blocks,¹¹ with each of these contributions depending only on the local environment. Moreover, long- and short-range electrostatic interactions are separated efficiently. Such an approach facilitates the design of superlattice structures of desired functionality by appropriate choice of the stacking sequence.^{12,13}

Even for bulk crystals, it turns out that working at fixed D is more convenient than working at fixed \mathcal{E} when considering materials that have ferroelectric instabilities.

(We now refer to three-dimensional field vectors.) The reason is that, in the region of the energy landscape near the unstable paraelectric configuration, the system is unstable to transformation into one of the ferroelectric domain states when working at fixed \mathcal{E} . The unstable paraelectric region of the $E(\mathbf{P})$ energy landscape is thus inaccessible using this approach. When working at fixed D , on the other hand, the internal energy $U(\mathbf{D})$ is typically found to be a single-valued function of D ,¹⁴ thus allowing access to the entire electric equation of state.¹⁵ Moreover, the second derivative of U with respect to D is directly related to the inverse capacitance of the material.⁸ When this quantity goes negative, it is a signature of the appearance of a ferroelectric instability, and indeed the magnitude of its negative value has been shown to be an insightful indicator of the strength of the ferroelectric instability.^{8,15} For example, it can play an important role in determining the critical thickness for ferroelectricity in capacitor nanostructures,¹¹ and its dependence on material structure and composition can be helpful in understanding the origin of the ferroelectric instability.

Up to now, applications of the fixed-displacement-field approach have been carried out using the private LAUTREC code package,¹⁶ in which the fixed- D constraint can be applied in only one Cartesian direction. In the present work, we have implemented the multidimensional fixed- D method in the context of the open-source ABINIT code package¹⁷ and demonstrates that it can be used to calculate the energy surface throughout the region of instability associated with the ferroelectric behavior, using PbTiO_3 as our prototypical material. By mapping the internal-energy landscape in the full three-dimensional D space, we can easily compare the energies of the competing ferroelectric states, trace the paths connecting these states, and compute the energy barriers along these paths. This approach therefore gives us a powerful tool for characterizing the ferroelectric be-

havior of a given material in all of its three-dimensional complexity in \mathbf{D} (or \mathcal{E} or \mathbf{P}) space.

The paper is organized as follows. In Sec. II, we briefly review the formalism for the fixed- \mathbf{D} calculations and describe our implementation. In Sec. III, we first test the implementation and compare with a previous calculation on PbTiO_3 . We also explore the internal energy landscape of PbTiO_3 in multidimensional \mathbf{D} space, and map out the relationships between the various field variables and their corresponding energy functionals. Finally, Sec. IV contains a summary and conclusions.

II. FORMALISM AND METHODOLOGY

We begin by briefly reviewing the fixed- \mathcal{E} and fixed- \mathbf{D} formalisms. For the former,^{1,2} the natural energy functional is the electric enthalpy

$$\mathcal{F}(\mathcal{E}, v) = E_{\text{KS}}(v) - \Omega \mathcal{E} \cdot \mathbf{P}(v), \quad (1)$$

while the fixed- \mathbf{D} method⁸ is naturally formulated in terms of the internal energy

$$U(\mathbf{D}, v) = E_{\text{KS}}(v) + \frac{\Omega}{8\pi} [\mathbf{D} - 4\pi\mathbf{P}(v)]^2. \quad (2)$$

In these equations Ω is the cell volume, v denotes the internal (ionic and electronic) coordinates, and E_{KS} is the ordinary zero-field Kohn-Sham energy functional.

To implement the fixed- \mathbf{D} method based on the above formalism, we have modified the open-source ABINIT code package, in which the fixed- \mathcal{E} calculation is already available.^{1,18} The key step is to update the electric field \mathcal{E} after each SCF iteration according to

$$\mathcal{E}_{n+1} = \lambda(\mathbf{D} - 4\pi\mathbf{P}_n) + (1 - \lambda)\mathcal{E}_n, \quad (3)$$

where \mathbf{P}_n and \mathcal{E}_n are polarization and electric field after the n 'th SCF iteration and λ is a damping parameter used to control the convergence speed. The iteration continues until the normal SCF convergence criterion is reached, and in addition, $|\mathbf{D} - 4\pi\mathbf{P}_n - \mathcal{E}_n|$ becomes less than a given tolerance.

Our calculations were performed within density-functional theory in the local-density approximation¹⁹ using norm-conserving pseudopotentials²⁰ and a plane-wave cutoff of 60 Ha. The pseudopotentials were the same as those of Ref 8. A $6 \times 6 \times 6$ Monkhorst-Pack grid²¹ was used to sample the Brillouin zone. The atomic coordinates of the five-atom unit cell were relaxed until all atomic force components were smaller than 10^{-5} Ha/Bohr, and the cell size and shape was varied until all stress components were below 10^{-7} Ha/Bohr³.

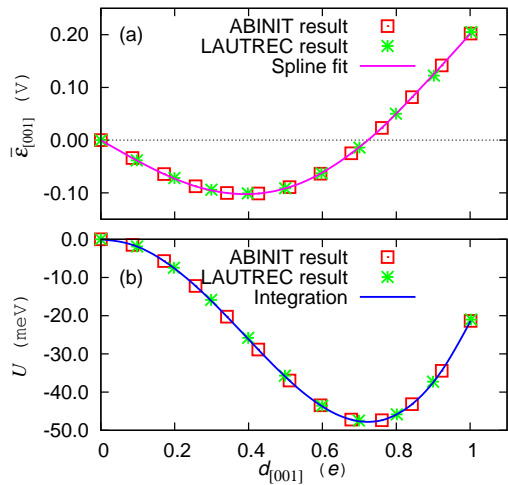


FIG. 1: (Color online) (a) Reduced electric field $\bar{\epsilon}$, and (b) internal energy U , as a function of reduced electric displacement field d along the [001] direction. The LAUTREC results are reproduced from Ref. 8. The solid curve in (a) is a cubic-spline fit to the ABINIT results; the solid curve in (b) is the numerical integral of the curve in (a).

III. RESULTS

A. Testing consistency

In order to test our implementation and compare the results with the previous calculation of Ref. 8, we have computed the internal energy U and the electric field \mathcal{E} as a function of D for the case that \mathbf{D} lies along the [001] axis. We started the calculation from the relaxed cubic structure (lattice constant of 3.88 Å) at $D = 0$, and increased D in steps of 0.02 a.u. At each D , the structure was fully relaxed with respect to both ionic positions and lattice parameters.

The results are plotted in Fig. 1(a), except that “reduced” field variables are used. That is, for each data point we computed the reduced electric field $\bar{\epsilon} = c\mathcal{E}$ and the reduced displacement field $d = a^2 D / 4\pi$, where a and c are the x - y and z lattice parameters respectively at the given value of D along [001]. In Fig. 1(b), we plot the internal energy U vs. reduced displacement field d . The previous results of Ref. 8, which were presented in terms of the same reduced variables, are also included in the plots. It is evident that the agreement between our Abinit calculation and the previous Lautrec one is excellent.

An advantage of using reduced variables in Fig. 1 is that d , $\bar{\epsilon}$, and U are related by the exact relation

$$\frac{\partial U}{\partial d} = \bar{\epsilon} \quad (4)$$

even when the relaxation of the lattice vectors with D is included.⁸ (By contrast, the corresponding relation be-

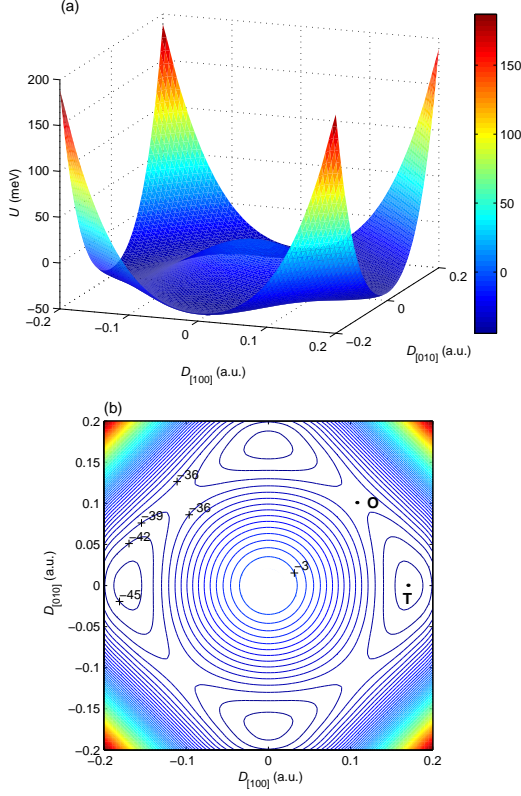


FIG. 2: (Color online) Internal energy surface $U(\mathbf{D})$ of PbTiO_3 plotted for \mathbf{D} lying in the plane spanned by the $[100]$ and $[010]$ directions. (a) Perspective plot. (b) Contour plot, with 3.0 meV separating contour levels. The minimum at T and saddle point at O represent spontaneously polarized tetragonal and orthorhombic states respectively.

tween D , \mathcal{E} , and U would require correction terms arising from derivatives of lattice vectors and cell volume.) To test whether our data is consistent with Eq. (4), we carried out a cubic spline fit of the $\bar{\epsilon}$ vs. d results to produce the solid curve shown in Fig. 1(a), and then integrated it numerically to obtain the solid curve shown in Fig. 1b. It can be seen that the internal energies coming directly from the Abinit calculations coincide quite precisely with those predicted by the application of Eq. (4).

These tests, which were repeated along other directions such as $[110]$ with equally good results, confirm the correctness and internal consistency of our computational implementation.

B. Internal energy in multidimensional \mathbf{D} space

We now explore the internal energy landscape of PbTiO_3 in three-dimensional \mathbf{D} space. While our calculations can be done for arbitrary \mathbf{D} , we restrict ourselves for presentation purposes to two-dimensional planes in \mathbf{D} space. We begin with the case of \mathbf{D} lying in the x - y plane.

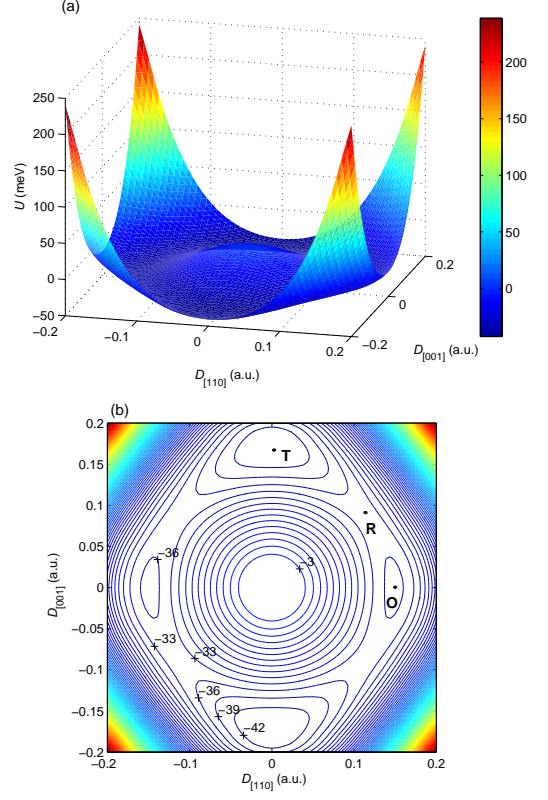


FIG. 3: (Color online) Internal energy surface $U(\mathbf{D})$ of PbTiO_3 plotted for \mathbf{D} lying in the plane spanned by the $[110]$ and $[001]$ directions. (a) Perspective plot. (b) Contour plot, with 3.0 meV separating contour levels. The minima at T and O and the saddle point at R represent spontaneously polarized tetragonal, orthorhombic, and rhombohedral states, respectively.

Recall that we already obtained relaxed solutions for a series of $D_{[100]}$ values increasing in increments of 0.02 a.u., up to 0.2 a.u., as described in the previous section. For each of these values of $D_{[100]}$, we use this solution as a starting structure as we apply $D_{[010]}$ in steps of 0.02 a.u., up to 0.2 a.u., while keeping $D_{[100]}$ constant. In other words, each equilibrium state is used as starting guess for its neighbor along y . In this way $U(\mathbf{D})$ is obtained on the specified grid in the quadrant with $D_{[100]} > 0$ and $D_{[010]} > 0$, and then symmetry is used to obtain the full internal-energy landscape.

The result is plotted in Fig. 2. Stationary points in such a diagram correspond to states with $\mathcal{E} = 0$. The four minima in the $\pm[001]$ and $\pm[010]$ directions correspond to four of the six tetragonal (T) ground states, at which P takes on its spontaneous value P_s and $D = 4\pi P_s$. There are also four saddle points along the $[110]$ and related directions, corresponding to states of orthorhombic (O) symmetry. The fact that these are higher in energy than the tetragonal minima just reflects the well-known fact that PbTiO_3 has a tetragonal ground state at $T = 0$.

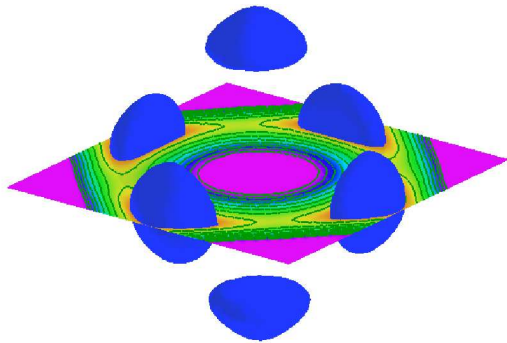


FIG. 4: (Color online) Dark blue: isosurfaces of $U(\mathbf{D})$ for PbTiO_3 plotted at $U = -44$ meV. Contoured plane: alternative view of data of Fig. 2(b).

The figure also shows that the energy differences are quite small along the valley connecting states $T \rightarrow O \rightarrow T$, relative to the large barrier that would have to be overcome if one were to pass through the origin of the figure. This is consistent with the work of Cohen and collaborators^{22–24} who pointed out how the easy rotation of the orientation of the polarization could lead to large piezoelectric responses, even if the energy landscape is relatively stiff with respect to changes in the magnitude of the polarization. Regarding the piezoelectric response of PbTiO_3 starting from its tetragonal ground state, the relative flatness of the energy landscape near state T in Fig. 2 along that path that would lead from $T \rightarrow O \rightarrow T$ is heuristically consistent with a relatively large observed value of the e_{15} piezoelectric constant in this material.²³

Fig. 3 shows corresponding plots for the plane spanning the $[110]$ and $[001]$ directions in three-dimensional \mathbf{D} space. The minima at the top and bottom of panel (b) are tetragonal states equivalent to those in Fig. 2. The apparent local minima at left and right in panel (b) are actually saddle points in three-dimensional \mathbf{D} space, and correspond to the orthorhombic states already discussed in connection with Fig. 2. We now also see four equivalent saddle points corresponding to a rhombohedral (R) state with the polarization along $[111]$ or related directions; these are points of double instability, in the sense that the Hessian of $U(\mathbf{D})$ has two negative eigenvalues. Once again, it is evident that there is a polarization rotation path via $T \rightarrow R \rightarrow O$ that is relatively low in energy compared to a direct polarization reversal passing through the paraelectric maximum at the origin.

The properties of PbTiO_3 at the tetragonal, orthorhombic and rhombohedral phases are summarized in Table I. The tetragonal phase has the lowest internal energy, followed by the orthorhombic and then the rhombohedral phase, consistent with previous studies and with the well-known fact that the ground state of PbTiO_3 is tetragonal. It can also be seen that the displacement field D_{\min} minimizing U and the corresponding spontaneous polarization $P_s = D_{\min}/4\pi$ decrease when going from T

TABLE I: Properties of PbTiO_3 in tetragonal (T), orthorhombic (O), and rhombohedral (R) phases. The cubic phase is chosen to define the zero of the internal energy U . D_{\min} is the displacement field at which U is a minimum, and P_s is the corresponding spontaneous polarization. The lattice vectors are also given.

	U (meV/cell)	D_{\min} (a.u.)	P_s (C/m ²)	a, b, c (Å)
T	-47.78	0.17	0.78	$a=3.85, c=4.03$
O	-39.80	0.15	0.68	$a=b=3.92, c=3.86$
R	-37.23	0.14	0.65	$a=3.90, \alpha=89.63^\circ$

to O to R, as might have been guessed from the fact that T is the deepest minimum while R is the shallowest.

To demonstrate the full 3D capabilities of the method, we also compute $U(\mathbf{D})$ on a 3D mesh of \mathbf{D} values in increments of $\Delta D_{[100]} = \Delta D_{[010]} = \Delta D_{[001]} = 0.04$ a.u. and use this data to plot the internal-energy isosurface at $U = -44$ meV shown in Fig. 4. The six isosurfaces surround the six equivalent internal-energy minima (at $U = -47.3$ meV) located along the $[001]$, $[010]$ and $[001]$ axes in \mathbf{D} space, providing a clear visualization of the six possible spontaneously-polarized domain states in tetragonal PbTiO_3 . The contour plane at $D_{[001]} = 0$ shows similar information as in Fig. 2(b). These results demonstrate the robustness of our implementation even in a fully multidimensional context.

C. Relations between field variables

The electric equation of state of a given crystalline insulator is given by specifying the relation between any two of the three field variables \mathbf{P} , \mathbf{D} , and \mathcal{E} , as for example by the functions $\mathcal{E}(\mathbf{D})$, $\mathbf{D}(\mathbf{P})$, or $\mathbf{P}(\mathcal{E})$. It is straightforward to convert between these using $\mathbf{D} = \mathcal{E} + 4\pi\mathbf{P}$. In our approach we obtain $\mathcal{E}(\mathbf{D})$ directly, and then generate $\mathbf{D}(\mathbf{P})$ or $\mathbf{P}(\mathcal{E})$ by numerical manipulation. In general the electric equation of state is a vector function of a vector, so to simplify our presentation we have calculated and plotted the electric equations of state only for cases in which all the field variables are constrained to lie along either the $[001]$, $[110]$, or $[111]$ axis.

The results are presented in Fig. 5, with the electric equations of state of the form $\mathcal{E}(D)$, $D(P)$, and $P(\mathcal{E})$ plotted in panels (a-c) respectively. The different curves correspond to plots along the $[001]$, $[110]$, or $[111]$ axis. We have also marked several special states on the diagrams for the case of the fields being along the $[001]$ axis. Proceeding from $1 \rightarrow 2 \rightarrow 3$ (or equivalently by symmetry from $1 \rightarrow 4 \rightarrow 5$), we pass from the cubic paraelectric State 1 to the spontaneously polarized tetragonal ferroelectric State 3. As the displacement field D increases in panel (b), the polarization P increases nearly linearly, while the electric field \mathcal{E} in panel (a) at first decreases to its minimum value (which defines State 2) and then

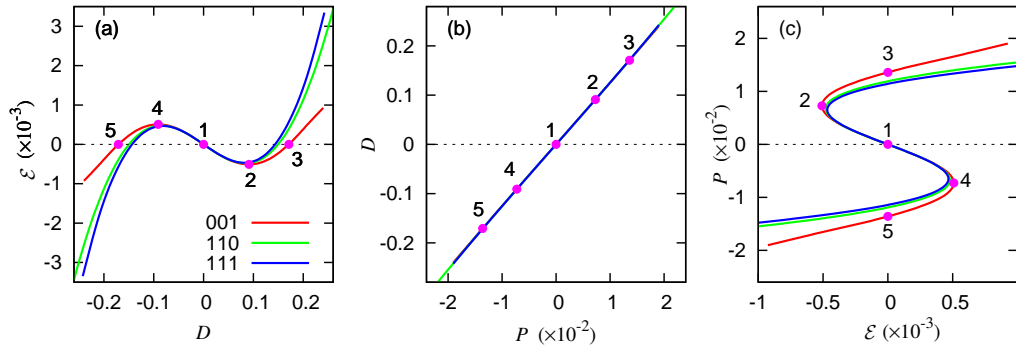


FIG. 5: (Color online) Electric equations of state of the form $\mathcal{E}(D)$ (a), $D(P)$ (b), and $P(\mathcal{E})$ (c), plotted for fields constrained to lie along the [001], [110] or [111] directions. All units are a.u. Numbered dots on the [001] curves indicate special states as described in the text.

increases and passes through zero at State 3. The plot of $P(\mathcal{E})$ in panel (c) takes the form of a hysteresis curve, but the portions of this curve in the region $4 \rightarrow 1 \rightarrow 2$ are unstable and therefore inaccessible under fixed- \mathcal{E} boundary conditions. This is a region in which the dielectric permittivity $\chi = \partial P / \partial \mathcal{E}$ is negative. The ability of the fixed- D method to explore this region of instability, which cannot be done using the fixed- \mathcal{E} method, is one of the important advantages of working at fixed D .⁸

Similar behaviors appear for D along the [110] or [111] directions. For these directions, States 1-5 are not marked, but are defined in the same way. The region of instability from State 1 to 2 is almost the same along all three directions, as can be seen in panels (a) and (c). In all cases, D is very nearly linear in P in panel (b). The main difference comes in the D and P values at the spontaneously-polarized State 3, which, as already discussed in connection with Table I, increase as we go from the [111] (R) to the [110] (O) to the [001] (T) directions. Also, \mathcal{E} increases much faster along [110] and [111] than along [001] after crossing the unstable State 2 in panel (a).

We emphasize that the hysteresis curves shown in Fig. 5(c) should not be compared directly with experiment. They correspond to the theoretical intrinsic hysteretic behavior that would occur if the entire crystal would switch coherently (i.e., maintaining full crystal periodicity at all times) from $+P_s$ to $-P_s$ on a path crossing through $P = 0$. This is a highly unrealistic picture of real ferroelectric switching, which usually proceeds by the motion of a domain wall between domains of different orientation of the polarization.²⁵ Our intrinsic coercive field of 2.5 MV/cm for the [001] case, which can be obtained from \mathcal{E} at State 2 in panel (a) or (c), is sure to be very much larger than the experimental one, which is most likely determined by pinning of domain walls to defects or by nucleation phenomena.

D. Relations between energy functionals

It is also instructive to see how the energy functionals behave as one traverses the trajectories shown in Fig. 5. Recall that the energy functionals that are naturally associated with field variables D , P , and \mathcal{E} are $U(D)$, $E_{KS}(P)$, and $\mathcal{F}(\mathcal{E})$; these are plotted in panels (a-c) of Fig. 6, respectively. Each plot again shows the behavior for fields constrained along either [001], [110], or [111], and the special States 1-5 are again marked for the [001] case.

The $U(D)$ and $E_{KS}(P)$ plots in panels (a-b) look remarkably similar after a rescaling of the horizontal axis by a factor of 4π . This is not surprising, since States 1, 3, and 5 have $\mathcal{E} = 0$, and are thus guaranteed to be extrema and to appear in exactly the same place in both panels (after 4π rescaling). The inflection points corresponding to States 2 and 4 are not located in quite the same place in both diagrams, but it is difficult to tell this by eye. Both panels clearly show a qualitatively similar double-well potential.

The $\mathcal{F}(\mathcal{E})$ curve in Fig. 6(c) looks complex, but its consistency with Fig. 5(c) can be checked through the relation $P = -\partial \mathcal{F} / \partial \mathcal{E}$, which follows from Eq. (1). Going through the unstable region from State 1 to State 2 in Fig. 6(c), \mathcal{E} becomes negative while $-\partial \mathcal{F} / \partial \mathcal{E}$ becomes positive, consistent with the corresponding behaviors of \mathcal{E} and P in Fig. 5(c). Then in the metastable region from State 2 to State 3, and into the stable region beyond State 3, \mathcal{E} returns to zero and then goes negative while $-\partial \mathcal{F} / \partial \mathcal{E}$ continues to grow more positive, again consistent with Fig. 5(c). The fact that \mathcal{F} diverges to $-\infty$ as $|\mathcal{E}|$ becomes large may look strange, but it is the normal behavior of $\mathcal{F}(\mathcal{E})$. For example, for a simple linear dielectric, $U(D)$ and $E_{KS}(P)$ are simple upright parabolas, while $\mathcal{F}(\mathcal{E})$ is an inverted parabola,⁸ and the asymptotic behaviors at large $|\mathcal{E}|$ are similar to those appearing in Fig. 6.

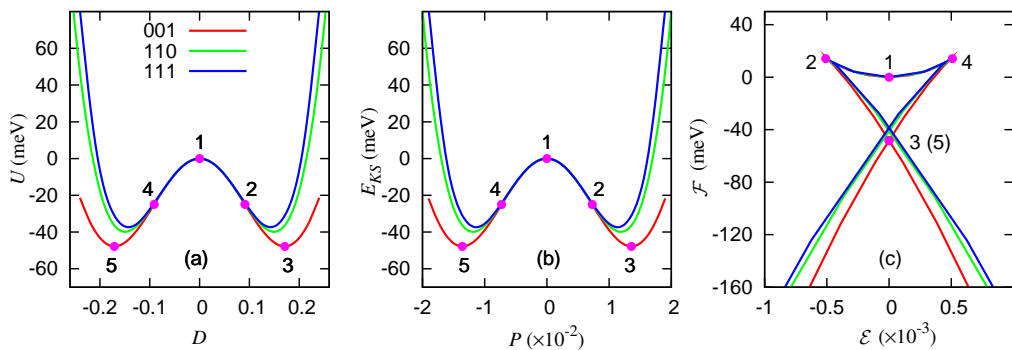


FIG. 6: (Color online) Energy functionals vs. their respective natural variables along [001], [110] and [111] directions: $U(D)$ (a), $E_{KS}(P)$ (b), and $\mathcal{F}(\mathcal{E})$ (c). All field variables are in units of a.u. Dots labeled 1-5 indicate the same special states as in Fig. 5.

IV. SUMMARY AND CONCLUSIONS

In summary, we have demonstrated the possibility of carrying out first-principles density-functional calculations under boundary conditions in which all three components of the electric displacement field \mathbf{D} are fixed. We have implemented the method in the open-source ABINIT software package.

Using PbTiO_3 as a prototypical system, we have explored the internal-energy landscape as a function of the full three-dimensional displacement-field vector. We have identified the minimum-energy tetragonal, orthorhombic and rhombohedral structures, and confirmed that the computed properties agree with previous first-principles studies. Our results allow for easy visualization of the low-energy paths for polarization rotation, known to be associated with large piezoelectric responses in this class of compounds. We have also presented the electric equa-

tions of state relating \mathcal{E} , D and P , as well as the corresponding energy functionals, along symmetry lines in \mathbf{D} space.

We hope that this fixed- \mathbf{D} approach may be useful for exploring the internal energy landscape of more complicated ferroelectric and dielectric materials, in bulk or superlattice form, as well as for studying domain-wall properties, piezoelectric and flexoelectric responses, field-driven phase transitions, and other phenomena in this important class of materials.

Acknowledgments

This work was supported by ONR Grant N00014-05-1-0054. We thank P. Ganesh and E. Murray for the help with code implementation. Computations were done at the Center for Piezoelectrics by Design.

* Electronic address: hongjiw10@physics.rutgers.edu

¹ I. Souza, J. Iniguez, and D. Vanderbilt, Phys. Rev. Lett. **89**, 117602 (2002).

² P. Umari and A. Pasquarello, Phys. Rev. Lett. **89**, 157602 (2002).

³ H. Fu and L. Bellaiche, Phys. Rev. Lett. **91**, 057601 (2003).

⁴ M. Veithen, X. Gonze, and Ph. Ghosez, Phys. Rev. Lett. **93**, 187401 (2004).

⁵ A. Antons, J. B. Neaton, Karin M. Rabe, and David Vanderbilt, Phys. Rev. B **71**, 024102 (2005).

⁶ M. Stengel and N.A. Spaldin, Phys. Rev. B **75**, 205121 (2007).

⁷ O. Dieguez and D. Vanderbilt, Phys. Rev. Lett. **96**, 056401 (2006).

⁸ M. Stengel, N.A. Spaldin, and D. Vanderbilt, Nat. Phys. **5**, 304 (2009).

⁹ M. Stengel, Phys. Rev. Lett. **106**, 136803 (2011)

¹⁰ M. Stengel and D. Vanderbilt, Phys. Rev. B **80**, 241103(R) (2009)

¹¹ M. Stengel, D. Vanderbilt, and N.A. Spaldin, Phys. Rev.

B **80**, 224110 (2009).

¹² X. Wu, M. Stengel, K.M. Rabe, and D. Vanderbilt, Phys. Rev. Lett. **101**, 087601 (2008)

¹³ X. Wu, K.M. Rabe, and D. Vanderbilt, Phys. Rev. B **83**, 020104(R) (2011)

¹⁴ In our experience this is always true for proper ferroelectrics, but not necessarily for improper ones.

¹⁵ M. Stengel, D. Vanderbilt and N.A. Spaldin, Nat. Mater. **8**, 392 (2009)

¹⁶ LAUTREC is a parallel “in-house” electronic-structure code developed primarily by M. Stengel.

¹⁷ X. Gonze, *et al.*, Comp. Mat. Sci. **25**, 478 (2002).

¹⁸ R.W. Nunes and X. Gonze, Phys. Rev. B **63**, 155107 (2001)

¹⁹ J.P. Perdew and Y. Wang, Phys. Rev. B **45**, 13244 (1992)

²⁰ N. Troullier and J.L. Martins, Phys. Rev. B **43**, 1993 (1991)

²¹ H.J. Monkhorst and J.D. Pack, Phys. Rev. B **13**, 5188 (1976)

²² H. Fu and R. E. Cohen, Nature **403**, 281 (2000).

²³ Z. Wu and R. E. Cohen, Phys. Rev. Lett. **95**, 037601

- (2005).
- ²⁴ P. Ganesh and R.E. Cohen, J. Phys.: Condens. Matter **21**, 064225 (2009).
- ²⁵ S. P. Beckman, Xinjie Wang, Karin M. Rabe, and David Vanderbilt, Phys. Rev. B **79**, 144124 (2009).